Chemical Science

ROYAL SOCIETY OF CHEMISTRY

EDGE ARTICLE

View Article Online
View Journal | View Issue

Cite this: *Chem. Sci.*, 2026, **17**, 8521

All publication charges for this article have been paid for by the Royal Society of Chemistry

Polymorphism-driven coordination geometry engineering for boosting nitrate electroreduction in Cu-pyrazolate chains

Zhanning Liu, †* Shanna An,† Qingzhong Xue * and Jian Tian *

Tailoring the coordination geometry of metal centers through polymorphism offers a powerful approach to isolating the structural origin of catalytic activity in metal–organic frameworks (MOFs). Herein, two copper-pyrazolate (Pz) polymorphs, **α-Cu(Pz)$_2$** and **β-Cu(Pz)$_2$** were synthesized, featuring identical chemical compositions and 1-periodic chain structures but distinct local coordination configurations. Remarkably, the **β-Cu(Pz)$_2$** exhibits a faradaic efficiency (FE) of 93.33% for the nitrate reduction reaction (NO_3RR), significantly outperforming **α-Cu(Pz)$_2$** (53.10%). Comprehensive structural analyses, *in situ* spectroscopy, and density functional theory (DFT) calculations revealed that the coordination geometry governs the electronic structure of the Cu active centers. Specifically, the *cis*-configured **β-Cu(Pz)$_2$** enables more delocalized Cu 3d orbitals and stronger Cu–O (NO_3^-) electronic coupling, thereby promoting nitrate adsorption and activation. This work demonstrates that MOF polymorphism allows precise tuning of electronic structures, offering a fundamental design principle for the development of advanced electrocatalysts toward sustainable nitrogen-cycle chemistry.

Received 1st December 2025
Accepted 8th March 2026

DOI: 10.1039/d5sc09385f

rsc.li/chemical-science

Introduction

Ammonia (NH_3) synthesis has been one of the largest chemical industries since the early twentieth century, owing to its crucial role in modern agriculture and its promising potential for energy storage.[1–4] Among the various strategies for NH_3 production, electrocatalytic synthesis *via* the nitrate reduction reaction (NO_3RR) has recently attracted increasing attention as a promising alternative to the energy-intensive Haber–Bosch process.[5–9] Moreover, by utilizing nitrate as the nitrogen feedstock, this approach integrates energy conversion with environmental remediation, providing a dual benefit for both ammonia synthesis and wastewater treatment.[10,11] Nevertheless, the reduction of NO_3^- to NH_3 is a complex process that involves the transfer of eight electrons and nine protons, accompanied by multiple hydrogenation and deoxygenation steps.[12] This intricate reaction pathway often leads to the formation of various intermediates and by-products.[13,14] Consequently, the rational design of efficient electrocatalysts and the elucidation of structural-performance relationships remain significant challenges.

Metal–organic frameworks (MOFs), a class of highly crystalline organic–inorganic hybrid materials, have recently emerged as an ideal platform for designing electrocatalysts and conducting mechanistic studies.[15–17] Their rich chemical diversity, facile functionalization, and modular architecture together provide a robust foundation for elucidating the molecular-level mechanisms underlying electrocatalytic processes. For instance, Cheng *et al.* demonstrated that introducing polar functional groups (–NH_2 or –NO_2) into ZIF-7 can enhance CO_2 capture and activation during electrocatalytic CO_2 reduction.[18] Zuo and coworkers reported that a bimetallic Zn_5-NiS_4TP MOF shows superior electrocatalytic NO_3RR performance,[19] in which the Zn_5 sites are responsible for reducing NO_3^- to NO_2^-, while [NiS_4] sites within the ligand facilitate the subsequent reduction of NO_2^- to NH_3. Our recent investigations have demonstrated that tuning the electron-withdrawing strength of halogen atoms (F, Cl, and Br) in the copper anilates can effectively modulate the electronic structure of Cu^{2+}, thereby facilitating the deoxygenation of *NO intermediate.[20,21] However, these strategies typically rely on introducing additional atoms or functional groups, which may complicate or obscure the precise elucidation of the intrinsic active sites.

Polymorphism, referring to the ability of a single compound to exist in two or more distinct crystalline forms,[22–24] is widely observed in MOFs. Subtle variations in the arrangement or coordination geometry of the building blocks can induce pronounced changes in their physical and chemical properties, offering a powerful platform for unraveling structure-property relationships.[25–27] For instance, the packing arrangement changes of ligand in cadmium squarates can induce dramatically different thermal expansion behaviors.[25] In Al-based MOFs, polymorphism arising from *cis-trans* configurations of

School of Materials Science and Engineering, Shandong Key Laboratory of Special Epoxy Resin, Shandong University of Science and Technology, Qingdao, 266590, China. E-mail: znliu@sdust.edu.cn; xueqz@upc.edu.cn; jiantian@sdust.edu.cn

† These authors contributed equally to this work.

μ-OH-connected $AlO_4(OH)_2$ chains leads to markedly different water adsorption behaviors.[27] However, its potential in electrocatalysis remains rarely explored. To this end, Cu^{2+} based MOFs provide an ideal model system, as Cu^{2+} centers not only exhibit a favorable alignment between the d-orbital energy levels and the LUMO π* of NO_3^-,[28] but also display diverse coordination modes that can give rise to rich polymorphic behavior.[29–31]

Motivated by these points and as a proof of concept, we herein systematically investigated the electrocatalytic NO_3RR performance of two 1-periodic copper-pyrazolate (**Pz**) polymorphs, **α-Cu(Pz)$_2$** and **β-Cu(Pz)$_2$**. Remarkably, the **β-Cu(Pz)$_2$** exhibits a significantly enhanced NO_3RR activity with the Faraday efficiency (FE) reaching 93.33%, while the **α-Cu(Pz)$_2$** only delivers a FE of 53.10%. Comprehensive analyses combining long-range and short-range structure investigations, *in situ* spectroscopic measurements, and density functional theory (DFT) calculations reveal that the coordination geometry of Cu centers plays a decisive role in modulating their electronic structures, thereby governing the adsorption and activation of nitrate species and ultimately determining the overall NO_3RR performance.

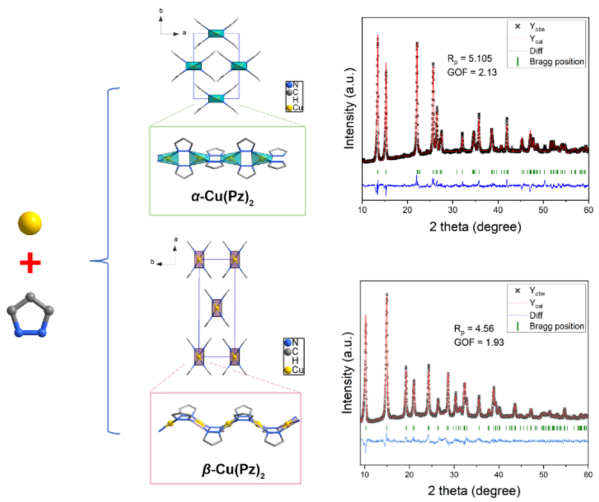

Fig. 1 Illustration of crystal structures of **α-Cu(Pz)$_2$** and **β-Cu(Pz)$_2$** and the corresponding Rietveld refinement patterns.

Results and discussion

The **α-Cu(Pz)$_2$** and **β-Cu(Pz)$_2$** phases were synthesized *via* soft-chemistry methods, and the detailed procedures are given in the SI.[32] Powder X-ray diffraction (PXRD) analyses, combined with Rietveld refinements (Fig. 1), confirmed that both products are phase pure and crystallize in distinct structures. Despite sharing the same chemical formula and both exhibiting infinite one-periodic (1p) chain motifs, their spatial arrangements are dramatically different. As shown in Fig. 1, the 1p chains in **α-Cu(Pz)$_2$** pack into an orthorhombic phase with the lattice parameters $a = 7.922$ Å, $b = 11.504$ Å, and $c = 7.791$ Å, whereas **β-Cu(Pz)$_2$** adopts a different unit cell with $a = 16.970$ Å, $b = 6.236$ Å, and $c = 7.294$ Å. The distinct packing modes stem from the local coordination differences within the 1p chain. In both samples, each Cu^{2+} is coordinated by four nitrogen atoms from four **Pz** ligands. However, in the **α-Cu(Pz)$_2$** phase, the **Pz** molecules adopt an alternating *trans* configuration, forming nearly

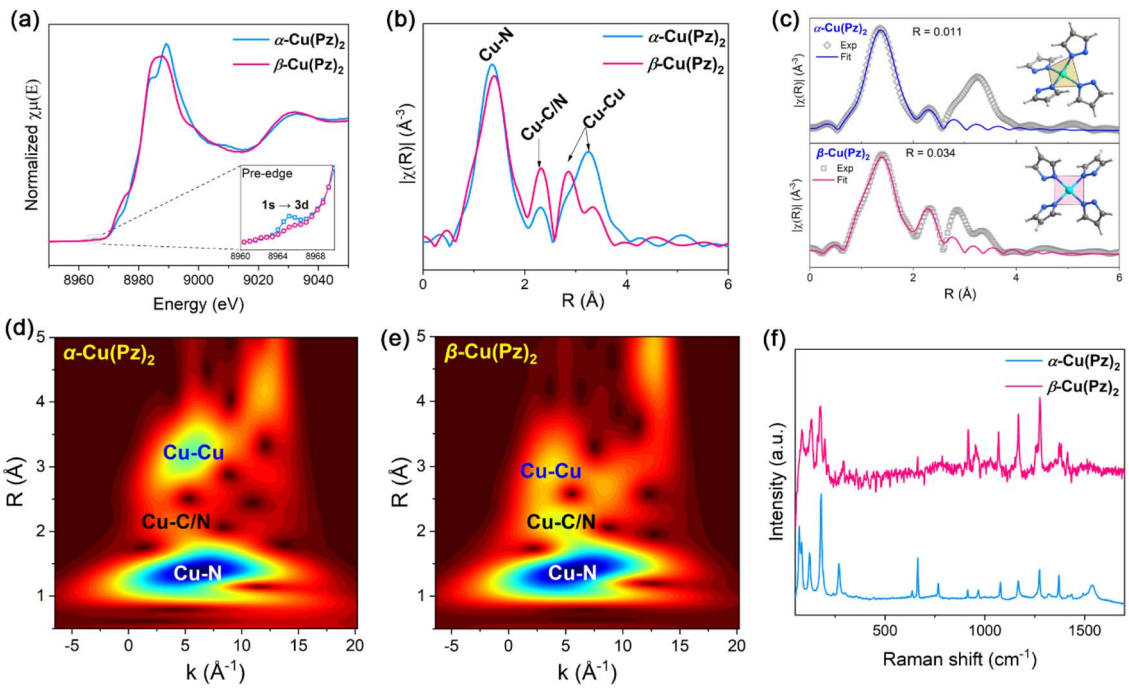

Fig. 2 (a) Cu K-edge XANES patterns of **α-Cu(Pz)$_2$** (blue) and **β-Cu(Pz)$_2$** (pink), and the inset shows the enlarged pre-edge region. (b and c) EXAFS patterns and the fitted results. (d and e) Wavelet transform contour plots of the two samples. (f) Raman spectra of **α-Cu(Pz)$_2$** (blue) and **β-Cu(Pz)$_2$** (pink).

linear 1p chains along the *a*-axis. In contrast, the **β-Cu(Pz)$_2$** phase displays a uniform *cis* configuration, in which the **Pz** molecules are oriented in the same direction, giving rise to a zig-zag chain conformation. Such distinct chain geometries induce different steric effects and packing behaviors, ultimately giving rise to the observed polymorphism of the **Cu(Pz)$_2$** system. The scanning electron microscope (SEM) images (Fig. S1) showed that both samples consist of nanosized particles with diameters in the range of 200–500 nm.

To gain atomic-level insight into the local coordination environments of **α-Cu(Pz)$_2$** and **β-Cu(Pz)$_2$** and to minimize potential effects from atomic occupancy disorder, Cu K-edge X-ray adsorption fine structure (XAFS) analyses were carried out. As shown in Fig. 2a, the X-ray absorption near-edge structure (XANES) spectra of the two compounds exhibit nearly identical adsorption edges, indicating that the Cu ions in both samples share similar oxidation states. This conclusion is further validated by the high-resolution X-ray photoelectron spectroscopy (XPS, Fig. S2), which confirms that the Cu ions in both samples are in the +2 oxidation state. Notably, the pre-edge peak at ~8965 eV is more pronounced in **α-Cu(Pz)$_2$** than in **β-Cu(Pz)$_2$**. Since this feature arises from the 1s → 3d electronic transition,[33–35] which is typically intensified in non-centrosymmetric coordination environments, the result indicates that the Cu^{2+} site in **α-Cu(Pz)$_2$** possesses a less symmetric local coordination environment. This was further supported by the extended X-ray absorption fine structure (EXAFS) analyses. As shown in Fig. 2b, the first peak at ~1.4 Å corresponds to the Cu–N bond, while the second coordination-shell peak at ~2.3 Å is attributed to Cu–C/N correlations arising from the next-nearest-neighbor C/N atoms of the **Pz** ligand. It should be noted that the EXAFS data are not phase-corrected, resulting in an apparent radial shift of approximately 0.4 Å relative to the actual Cu–N distances.[36] The EXAFS fitting results reveal that Cu^{2+} in both compounds is four-coordinate (Tables S1 and S2). However, the coordination geometries differ distinctly, being a distorted tetrahedron in **α-Cu(Pz)$_2$** and a square-planar configuration in **β-Cu(Pz)$_2$** (Fig. 2c). According to the Cambridge Crystallographic Data Centre (CCDC), most of the Cu(II)-N_4 based complexes preferentially adopt a square-planar

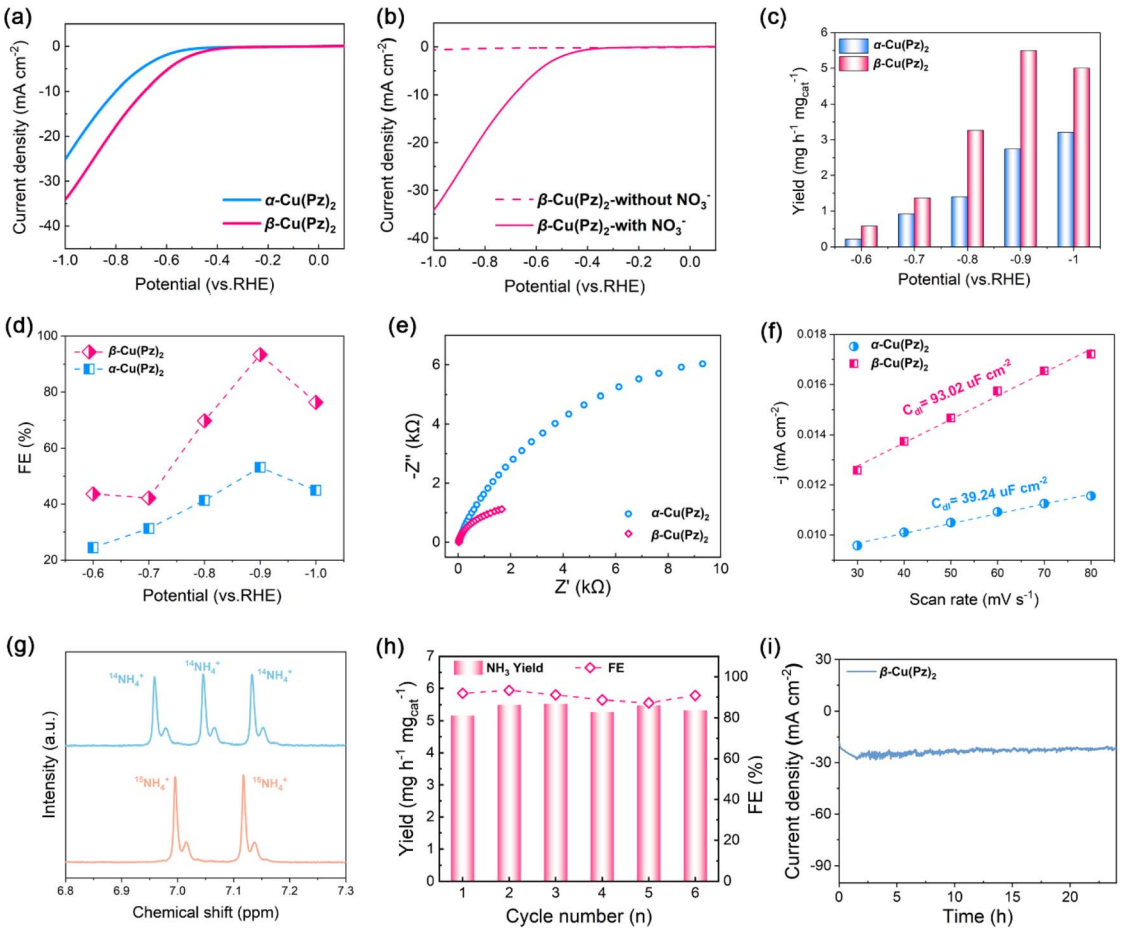

Fig. 3 (a) LSV curves for **α-Cu(Pz)$_2$** (blue) and **β-Cu(Pz)$_2$** (pink) in the electrolyte. (b) Comparison of LSV curves for **β-Cu(Pz)$_2$** recorded with (solid line) and without (dashed line) NO_3^-. (c and d) NH_3 yield rates and corresponding FEs of **α-Cu(Pz)$_2$** (blue) and **β-Cu(Pz)$_2$** (pink) at different potentials. (e and f) EIS and ECSA measurements of the two samples. (g) ^{1}H NMR spectra of the products after NO_3RR over **β-Cu(Pz)$_2$** using $K^{14}NO_3$ (blue) and $K^{15}NO_3$ (orange) as the feeding nitrogen sources. (i) Cycling stability tests of **β-Cu(Pz)$_2$** at −0.9 V (*vs.* RHE) for 6 cycles. (h) Time-dependent current density curve at −0.9 V (*vs.* RHE) for over 24 h for **β-Cu(Pz)$_2$**.

geometry. Thus, the distorted tetrahedral coordination environment in **α-Cu(Pz)$_2$** may render this phase metastable. Further DFT calculations showed that, the ground-state energy of **β-Cu(Pz)$_2$** is significantly lower than **α-Cu(Pz)$_2$** with $\Delta E_0 = -0.12775$ eV (Table S3), confirming the higher intrinsic stability of **β-Cu(Pz)$_2$**. Fig. 2d and e display the wavelet transform (WT) contour plots of the two samples. The lobes observed at ~5 Å^{-1} and ~3 Å are assigned to the third coordination sphere, corresponding to Cu–Cu pairs. Obviously, the Cu–Cu distance in **α-Cu(Pz)$_2$** is longer than that in **β-Cu(Pz)$_2$**, which is consistent with the quasi-linear and zig-zag configurations observed in their long-range structures. Moreover, the Raman spectra of the two compounds show similar characteristic bands (Fig. 2f), validating their identical building blocks.

Electrocatalytic NO_3RR performances of the two polymorphs were evaluated in a typical H-type electrolytic cell containing 0.1 M Na_2SO_4 and 0.1 M KNO_3. The linear sweep voltammetry (LSV) curves of **α-Cu(Pz)$_2$** and **β-Cu(Pz)$_2$** are shown in Fig. 3a. The current density of **β-Cu(Pz)$_2$** is obviously higher than that of **α-Cu(Pz)$_2$** at the same potential, inferring its higher electrocatalytic activity. In addition, the pronounced increase in current density in the presence of NO_3^- confirms its electrocatalytic NO_3RR performance (Fig. 3b). Based on the LSV results, a series of NO_3RR measurements were conducted under different potentials ranging from −0.5–−1.0 V *vs.* RHE. The NH_3 yield rates were quantified using a chronopotentiometry method (Fig. S3–S5). As shown in Fig. 3c and d, both NH_3 yield rates and FEs display a volcanic trend with increasingly negative potentials. At all applied potentials, **β-Cu(Pz)$_2$** outperforms **α-Cu(Pz)$_2$**. Remarkably, at −0.9 V *vs.* RHE, **β-Cu(Pz)$_2$** achieves an NH_3 yield rate of 5.50 mg h^{-1} mg$_{cat}^{-1}$ with an FE of 93.33%, nearly twice that of **α-Cu(Pz)$_2$** (2.74 mg h^{-1} mg$_{cat}^{-1}$ and 53.10%) and outperforming most of the reported copper-based electrocatalysts (Table S3). These results indicate that changes in the local coordination geometry of the microenvironment exert a significant regulatory effect on the catalytic performance. To confirm the origin of ammonia production, isotope labeling experiments were performed. As shown in Fig. 3g, the ^{1}H nuclear magnetic resonance (NMR) spectra using $^{15}NO_3^-$ as the feeding nitrogen source display the characteristic doublet of $^{15}NH_4^+$, whereas $^{14}NO_3^-$ produces $^{14}NH_4^+$ with a triplet signal. These results confirm that the NH_4^+ detected in the electrolyte does originate from nitrate reduction rather than other impurities. Besides, the electrochemical impedance spectroscopy (EIS) measurements were conducted to assess the conductivity of electrodes. As shown in Fig. 3e, the **β-Cu(Pz)$_2$** exhibits a significantly lower interfacial electron-transfer resistance. Meanwhile, the electrochemically active surface area (ECSA) measurements (Fig. 3f, S6) indicate that **β-Cu(Pz)$_2$** has a higher C_{dl} value of 93.02 μF cm^{-2}, obviously exceeding that of **α-Cu(Pz)$_2$** (39.24 μF cm^{-2}), suggesting a greater number of accessible active sites in **β-Cu(Pz)$_2$**. The cycling performance of **β-Cu(Pz)$_2$** was evaluated at −0.9 V *vs.* RHE. Over six consecutive cycles, no significant decrease in NH_3 yield rate or FE can be observed (Fig. 3h), and negligible metal ion leaching was detected. Moreover, the 24 h time-dependent current density profile shows negligible decay (Fig. 3i), further confirming its long-term stability and potential for practical applications.

In situ Fourier transform infrared (FTIR) spectroscopy was employed to probe the possible reaction intermediates formed during the ammonia synthesis process over **α-Cu(Pz)$_2$** and **β-Cu(Pz)$_2$** catalysts. As shown in Fig. 4a and b, both catalysts exhibit similar intermediate-related signals as the applied potential shifts from open-circuit potential (OCP) to −1.0 V *vs.* RHE. Among them, the band at 1404 cm^{-1} is attributed to the adsorbed NO_3^- species, while the bands at 1205 cm^{-1}, 1537 cm^{-1}, and 1285 cm^{-1} correspond to the formed *NO_2, *NO, and *NH_2 intermediates,[37,38] respectively. These characteristic peaks suggest that the electrocatalytic NO_3RR proceeds through a successive deoxygenation and hydrogenation process. Notably, the intermediate-related IR bands of **β-Cu(Pz)$_2$** exhibit a markedly higher signal-to-noise ratio than those of **α-Cu(Pz)$_2$**, implying enhanced catalytic performance. This observation is fully consistent with its superior NO_3RR performance described above. Furthermore, *in situ* Raman spectra were used to detect the possible structural changes in the catalysts (Fig. 4c and d). Under the applied potentials, no additional Raman bands were observed, confirming the structural stability of the catalysts.

Subsequently, guided by the above *in situ* spectroscopic results, density functional theory (DFT) calculations were carried out to further elucidate the origin of their distinct catalytic activities (Fig. S7 and S8). The electrocatalytic NO_3RR

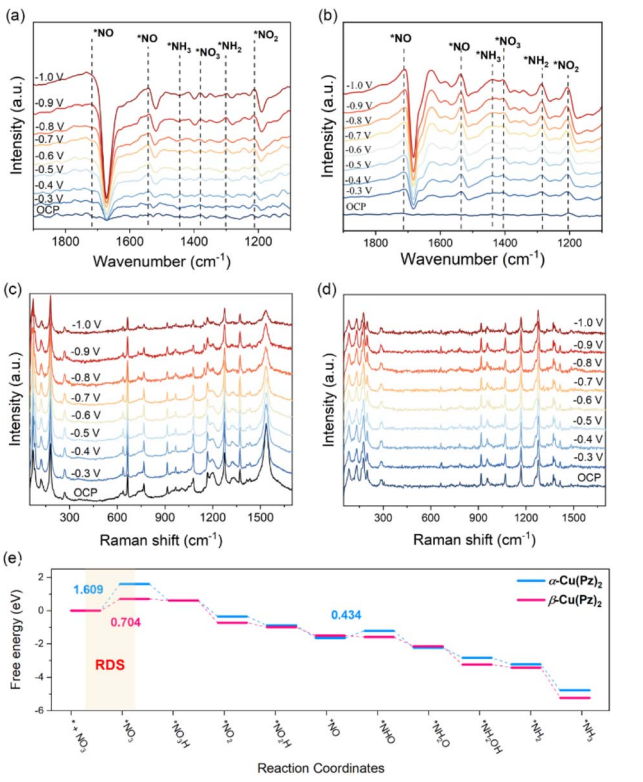

Fig. 4 *In situ* FTIR and Raman spectra of **α-Cu(Pz)$_2$** (a and c) and **β-Cu(Pz)$_2$** (b and d). (e) Calculated Gibbs free energy diagram along the catalytic reaction pathway on **α-Cu(Pz)$_2$** (blue) and **β-Cu(Pz)$_2$** (pink).

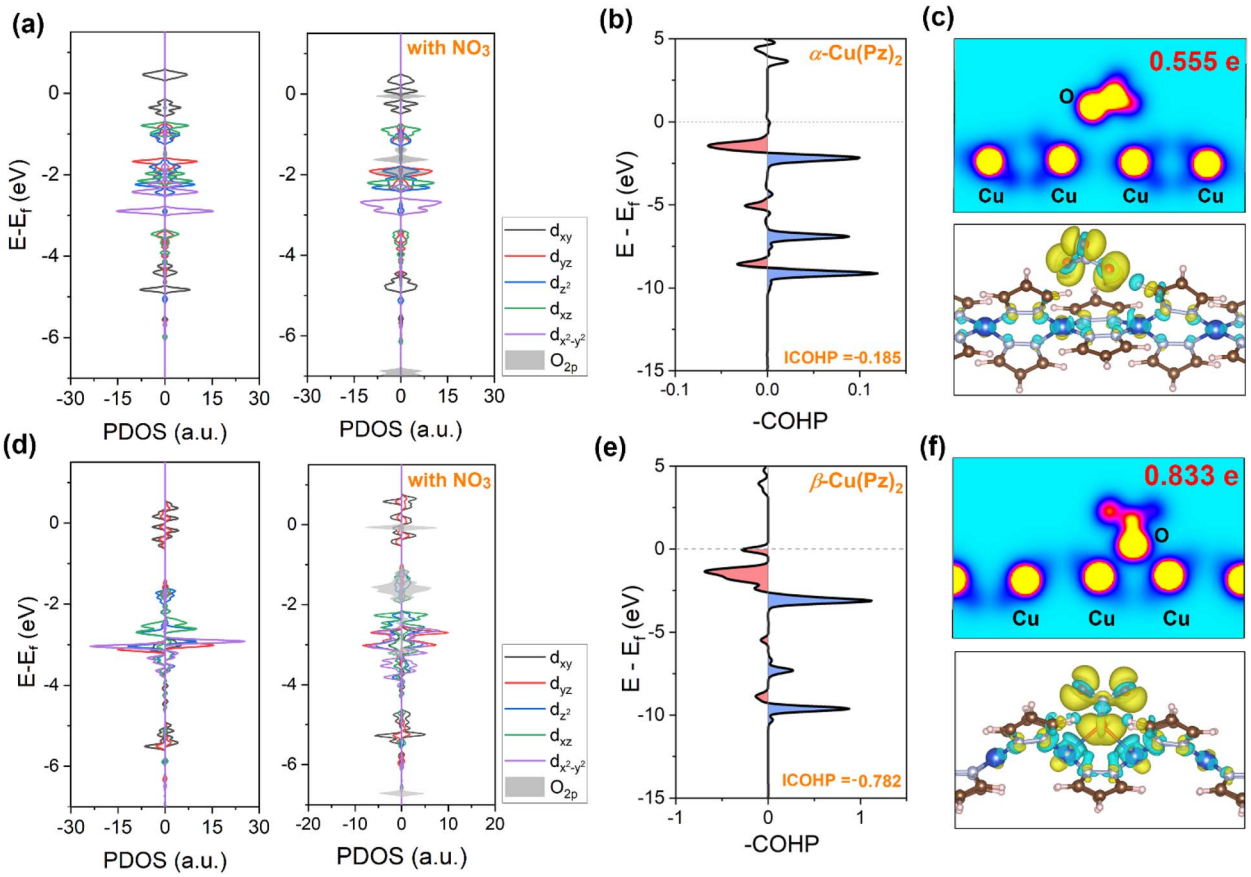

Fig. 5 (a and d) Spin-polarized PDOS of **α-Cu(Pz)$_2$** and **β-Cu(Pz)$_2$** before (left) and after (right) nitrate adsorption. (b and e) COHP curves and corresponding ICOHP values for the Cu–O bonds. (c and f) Charge density difference cross-sectional slices (top) and isosurface maps of nitrate adsorbed **α-Cu(Pz)$_2$** and **β-Cu(Pz)$_2$**.

process primarily proceeds through the following pathway: (1) adsorption and activation of NO_3^- to form *NO_3 radical; (2) successive deoxygenation to produce *NO and stepwise hydrogenation *via* proton-coupled electron transfer (PCET) to ultimately generate *NH_3.[39] As depicted in the free energy profiles (Fig. 4e), NO_3^- adsorption is the rate-determining step (RDS) throughout the overall reaction process for both catalysts. The corresponding energy barrier on **β-Cu(Pz)$_2$** (ΔG = 0.704 eV) is significantly lower than that on **α-Cu(Pz)$_2$** (ΔG = 1.609 eV), indicating a more favourable activation of the NO_3^- species. To gain deeper insight into this difference, the electronic structures and orbital interactions of the two catalysts were examined. The projected density of states (PDOS) of Cu 3d orbitals for pristine **α-Cu(Pz)$_2$** and **β-Cu(Pz)$_2$** are shown in Fig. 5a and d. In **α-Cu(Pz)$_2$**, the Cu 3d states are relatively localized, with narrow distributions and weak overlap, indicating limited hybridization with the surrounding ligand orbitals. In contrast, **β-Cu(Pz)$_2$** exhibits broader and more continuous 3d states, implying enhanced delocalization and stronger Cu-ligand electronic coupling. Upon NO_3^- adsorption, **β-Cu(Pz)$_2$** displays a more pronounced overlap between the O 2p orbitals of NO_3^- and the Cu 3d orbitals, revealing stronger Cu–O electronic coupling and greater charge transfer capability. This conclusion is further supported by the integrated crystal orbital Hamilton population (ICOHP) analysis, where the Cu–O bonds in **α-Cu(Pz)$_2$** and **β-Cu(Pz)$_2$** with adsorbed NO_3^- are −0.185 eV and −0.782 eV (Fig. 5b and e), respectively. The more negative ICOHP value signifies a stronger chemical bonding interaction,[40] corroborating that the *NO_3 binds more tightly to **β-Cu(Pz)$_2$** than to **α-Cu(Pz)$_2$**. The charge density difference maps (Fig. 5c and f) also demonstrate that the NO_3^- species gains approximately 0.555 e and 0.833 e from **α-Cu(Pz)$_2$** and **β-Cu(Pz)$_2$**, respectively, confirming more significant charge transfer in the latter. Overall, these results reveal that the enhanced NO_3RR performance of **β-Cu(Pz)$_2$** originates from its stronger Cu–O orbital hybridization and greater electron delocalization, which can effectively facilitate the NO_3^- activation and reduction.

Conclusions

In summary, two copper-pyrazolate polymorphs **α-Cu(Pz)$_2$** and **β-Cu(Pz)$_2$** were successfully synthesized. Both samples feature 1-periodic chain structures, while their local coordination geometry were dramatically different, with **α-Cu(Pz)$_2$** adopting a *trans* configuration and **β-Cu(Pz)$_2$** adopting a *cis* configuration. Electrocatalytic NO_3RR measurements revealed that the **β-Cu(Pz)$_2$** demonstrates a markedly superior performance, achieving a FE of 93.33%, compared with 53.10% of **α-Cu(Pz)$_2$**.

This enhancement originates from their distinct electronic structures. In **β-Cu(Pz)$_2$**, the Cu 3d orbitals are more delocalized, enabling greater electron donation to the adsorbed *NO_3 species, thereby promoting the nitrate adsorption, activation, and subsequent reduction. These findings highlight the crucial role of coordination geometry engineering in tuning the electronic properties of active metal centers, providing valuable insights for the rational design of advanced electrocatalysts for sustainable ammonia synthesis and beyond.

Author contributions

Conceptualization, Zhanning Liu; methodology and investigation, Zhanning Liu, and Shanna An; software, Zhanning Liu, Qingzhong Xue, and Jian Tian; funding acquisition, Zhanning Liu; resources, Qingzhong Xue and Jian Tian. All authors have read and agreed to the published version of the manuscript.

Conflicts of interest

There are no conflicts to declare.

Data availability

The data underlying this study are available in the published article and its supplementary information (SI). Supplementary information: experimetnal details, DFT calculations, SEM, XPS, electrochemical measurement results, and crystal structure models. See DOI: https://doi.org/10.1039/d5sc09385f.

Acknowledgements

This work was supported by the National Natural Science Foundation of China (No. 22005340), Natural Science Foundation of Shandong Province (No. ZR2022JQ21), National Ten Thousand Talent Program for Young Top-notch Talents, Science and Technology Special Project of Qingdao City (No. 25-1-5-cspz-9-nsh), and Qingdao Natural Science Foundation (24-4-4-zrjj-194-jch).

Notes and references

1 D. R. MacFarlane, P. V. Cherepanov, J. Choi, B. H. Suryanto, R. Y. Hodgetts, J. M. Bakker, F. M. F. Vallana and A. N. Simonov, A roadmap to the ammonia economy, *Joule*, 2020, **4**, 1186–1205.

2 K. Zhang, A. Cao, L. H. Wandall, J. Vernieres, J. Kibsgaard, J. K. Nørskov and I. Chorkendorff, Spin-mediated promotion of Co catalysts for ammonia synthesis, *Science*, 2024, **383**, 1357–1363.

3 M. Wang, M. A. Khan, I. Mohsin, J. Wicks, A. H. Ip, K. Z. Sumon, C.-T. Dinh, E. H. Sargent, I. D. Gates and M. G. Kibria, Can sustainable ammonia synthesis pathways compete with fossil-fuel based Haber–Bosch processes?, *Energy Environ. Sci.*, 2021, **14**, 2535–2548.

4 S. Wu, N. Salmon, M. M.-J. Li, R. Bañares-Alcántara and S. C. E. Tsang, Energy decarbonization via green H_2 or NH_3?, *ACS Energy Lett.*, 2022, **7**, 1021–1033.

5 S. Li, X. Fu, J. K. Nørskov and I. Chorkendorff, Towards sustainable metal-mediated ammonia electrosynthesis, *Nat. Energy*, 2024, **9**, 1344–1349.

6 P. H. van Langevelde, I. Katsounaros and M. T. Koper, Electrocatalytic nitrate reduction for sustainable ammonia production, *Joule*, 2021, **5**, 290–294.

7 J. Liang, Z. Li, L. Zhang, X. He, Y. Luo, D. Zheng, Y. Wang, T. Li, H. Yan and B. Ying, Advances in ammonia electrosynthesis from ambient nitrate/nitrite reduction, *Chem*, 2023, **9**, 1768–1827.

8 M. A. Mushtaq, A. Kumar, W. Liu, Q. Ji, Y. Deng, G. Yasin, A. Saad, W. Raza, J. Zhao and S. Ajmal, A metal coordination number determined catalytic performance in manganese borides for ambient electrolysis of nitrogen to ammonia, *Adv. Mater.*, 2024, **36**, 2313086.

9 Y.-C. Liu, J.-R. Huang, H.-L. Zhu, X.-F. Qiu, C. Yu, X.-M. Chen and P.-Q. Liao, Electrosynthesis of pure urea from pretreated flue gas in a proton-limited environment established in a porous solid-state electrolyte electrolyser, *Nat. Nanotechnol.*, 2025, 1–7.

10 Y. Du, H. Lu, J. Wu, Y. Zou, Z. F. Huang, J. J. Zou, T. Mu, J. Gao, X. D. Zhu and Y. C. Zhang, Selenium-Deficient $FeSe_2/Fe_3O_4$ Electrocatalyst for Nitrate Reduction to Ammonia, *Angew. Chem., Int. Ed.*, 2025, **64**, e202420903.

11 D.-S. Huang, X.-F. Qiu, J.-R. Huang, M. Mao, L. Liu, Y. Han, Z.-H. Zhao, P.-Q. Liao and X.-M. Chen, Electrosynthesis of urea by using Fe2O3 nanoparticles encapsulated in a conductive metal–organic framework, *Nat. Synth.*, 2024, **3**, 1404–1413.

12 P. Muthukumar, Z. Ullah, X. Zhang, H. Ullah, Y. Liu, L. Li, S. Tian, X. Zhou, S. P. Anthony, Y. Zuo, C. Lv, X. Wang and C. Wang, Unlocking a Water Coordination Environment in Co-Based Metal–Organic Frameworks for Advanced Nitrate-to-Ammonia Electroreduction, *J. Am. Chem. Soc.*, 2025, **147**, 29949.

13 H. Xu, Y. Ma, J. Chen, W.-X. Zhang and J. Yang, Electrocatalytic reduction of nitrate–a step towards a sustainable nitrogen cycle, *Chem. Soc. Rev.*, 2022, **51**, 2710–2758.

14 G. Zhang, X. Li, K. Chen, Y. Guo, D. Ma and K. Chu, Tandem electrocatalytic nitrate reduction to ammonia on MBenes, *Angew. Chem., Int. Ed.*, 2023, **62**, e202300054.

15 Z. Yang, A. Li, H. Li, G. Lai, Y. Fu, Y. Zhang, K. Wang, S. Zeng, L. Xie and M. Li, Dimensionality Reduction of Metal–Organic Frameworks to Monolayers for Enhanced Electrocatalysis, *Angew. Chem., Int. Ed.*, 2025, e202505399.

16 N. Sun, S. S. A. Shah, Z. Lin, Y.-Z. Zheng, L. Jiao and H.-L. Jiang, MOF-based electrocatalysts: an overview from the perspective of structural design, *Chem. Rev.*, 2025, **125**, 2703–2792.

17 A. H. Mamaghani, J. Liu, Z. Zhang, R. Gao, Y. Wu, H. Li, M. Feng and Z. Chen, Promises of MOF-based and MOF-derived materials for electrocatalytic CO_2 reduction, *Adv. Energy Mater.*, 2024, **14**, 2402278.

18 J. Chen, G. Wang, Y. Dong, J. Ji, L. Li, M. Xue, X. Zhang and H. M. Cheng, Controlling the Polarity of Metal–Organic Frameworks to Promote Electrochemical CO_2 Reduction, *Angew. Chem., Int. Ed.*, 2025, **64**, e202416367.

19 Z. Zhang, Y. Lv, Y. Gu, X. Zhou, B. Tian, A. Zhang, Z. Yang, S. Chen, J. Ma and M. Ding, Dual Zn_5-NiS_4 Sites in a Redox-Active Metal–Organic Framework Enables Efficient Cascade Catalysis for Nitrate-to-Ammonia Conversion, *Angew. Chem., Int. Ed.*, 2025, **64**, e202418272.

20 C. Xing, J. Ren, L. Fan, J. Zhang, M. Ma, S. Wu, Z. Liu and J. Tian, π-d conjugated copper chloranilate with distorted Cu-O_4 site for efficient electrocatalytic ammonia production, *Adv. Funct. Mater.*, 2024, **34**, 2409064.

21 Z. Liu, C. Xing, Y. Shan, M. Ma, S. Wu, R. Ge, Q. Xue and J. Tian, Molecular engineering of 1D conjugated copper anilate coordination polymers for boosting electrocatalytic nitrate reduction to ammonia, *Chem. Sci.*, 2025, **16**, 7010–7017.

22 A. J. Cruz-Cabeza and J. Bernstein, Conformational polymorphism, *Chem. Rev.*, 2014, **114**, 2170–2191.

23 B. Karadeniz, D. Žilić, I. Huskić, L. S. Germann, A. M. Fidelli, S. Muratović, I. Lončarić, M. Etter, R. E. Dinnebier and D. Barišić, Controlling the polymorphism and topology transformation in porphyrinic zirconium metal–organic frameworks via mechanochemistry, *J. Am. Chem. Soc.*, 2019, **141**, 19214–19220.

24 T. J. Matemb Ma Ntep, M. Wahiduzzaman, E. Laurenz, I. Cornu, G. Mouchaham, I. Dovgaliuk, S. Nandi, K. Knop, C. Jansen and F. Nouar, When polymorphism in metal–organic frameworks enables water sorption profile tunability for enhancing heat allocation and water harvesting performance, *Adv. Mater.*, 2024, **36**, 2211302.

25 Z. Liu, R. Ma, J. Deng, J. Chen and X. Xing, Molecular packing-dependent thermal expansion behaviors in metal squarate frameworks, *Chem. Mater.*, 2020, **32**, 2893–2898.

26 Z. Chen, C.-H. Ho, X. Wang, S. M. Vornholt, T. M. Rayder, T. Islamoglu, O. K. Farha, F. Paesani and K. W. Chapman, Humidity-responsive polymorphism in CALF-20: a resilient MOF physisorbent for CO_2 capture, *ACS Mater. Lett.*, 2023, **5**, 2942–2947.

27 T. J. Matemb Ma Ntep, M. Wahiduzzaman, E. Laurenz, I. Cornu, G. Mouchaham, I. Dovgaliuk, S. Nandi, K. Knop, C. Jansen, F. Nouar, P. Florian, G. FuIdner, G. Maruin, C. Janiak and C. Serre, When polymorphism in metal-organic frameworks enables water sorption profile tunability for enhancing heat allocation and water harvesting performance, *Adv. Mater.*, 2024, **36**, 2211302.

28 G.-F. Chen, Y. Yuan, H. Jiang, S.-Y. Ren, L.-X. Ding, L. Ma, T. Wu, J. Lu and H. Wang, Electrochemical reduction of nitrate to ammonia via direct eight-electron transfer using a copper–molecular solid catalyst, *Nat. Energy*, 2020, **5**, 605–613.

29 Y. Yang, C. Zhang, C. Zhang, Y. Shi, J. Li, B. Johannessen, Y. Liang, S. Zhang, Q. Song and H. Zhang, Ligand-tuning copper in coordination polymers for efficient electrochemical C–C coupling, *Nat. Commun.*, 2024, **15**, 6316.

30 J. Jiao, X. Kang, J. Yang, S. Jia, Y. Peng, S. Liu, C. Chen, X. Xing, M. He and H. Wu, Steering the reaction pathway of CO2 electroreduction by tuning the coordination number of copper catalysts, *J. Am. Chem. Soc.*, 2024, **146**, 15917–15925.

31 Z.-H. Zhao, J.-R. Huang, P.-Q. Liao and X.-M. Chen, Highly efficient electroreduction of CO_2 to ethanol via asymmetric C–C coupling by a metal–organic framework with heterodimetal dual sites, *J. Am. Chem. Soc.*, 2023, **145**, 26783–26790.

32 A. Cingoani, S. Galli, N. Mascicchi, L. Pandolfo, C. Pettinari and A. Sironi, Sorption-desorption behavior of bispyrazolato-copper(II) 1D coordination polymers, *J. Am. Chem. Soc.*, 2005, **127**, 6144–6145.

33 B. L. Geoghegan, Y. Liu, S. Peredkov, S. Dechert, F. Meyer, S. DeBeer and G. E. Cutsail III, Combining valence-to-core x-ray emission and Cu k-edge x-ray absorption spectroscopies to experimentally assess oxidation state in organometallic Cu (I)/(II)/(III) complexes, *J. Am. Chem. Soc.*, 2022, **144**, 2520–2534.

34 L. León-Alcaide, C. Castillo-Blas, V. Martin-Diaconescu, I. Da Silva, D. A. Keen, T. D. Bennett and G. M. Espallargas, Solvent-free approach for the synthesis of heterometallic Fe–Zn-ZIF glass via a melt-quenched process, *Chem. Sci.*, 2025, **16**, 7946–7955.

35 F. Farges, Ab initio and experimental pre-edge investigations of the Mn K-edge XANES in oxide-type materials, *Phys. Rev. B*, 2005, **71**, 155109.

36 V. L. Sushkevich, O. V. Safonova, D. Palagin, M. A. Newton and J. A. van Bokhoven, Structure of copper sites in zeolites examined by Fourier and wavelet transform analysis of EXAFS, *Chem. Sci.*, 2020, **11**, 5299–5312.

37 X. Gu, J. Zhang, S. Guo, Y. Zhang, L. Xu, R. Jin and G. Li, Tiara Ni Clusters for Electrocatalytic Nitrate Reduction to Ammonia with 97% Faradaic Efficiency, *J. Am. Chem. Soc.*, 2025, **14**, 22785.

38 L. Zhou, X. Chen, S. Zhu, K. You, Z. J. Wang, R. Fan, J. Li, Y. Yuan, X. Wang and J. Wang, Two-dimensional Cu Plates with Steady Fluid Fields for High-rate Nitrate Electroreduction to Ammonia and Efficient Zn-Nitrate Batteries, *Angew. Chem., Int. Ed.*, 2024, **136**, e202401924.

39 D. R. Weinberg, C. J. Gagliardi, J. F. Hull, C. F. Murphy, C. A. Kent, B. C. Westlake, A. Paul, D. H. Ess, D. G. McCafferty and T. J. Meyer, Proton-coupled electron transfer, *Chem. Rev.*, 2012, **112**, 4016–4093.

40 S. Wang, Q. Jiang, S. Ju, C.-S. Hsu, H. M. Chen, D. Zhang and F. Song, Identifying the geometric catalytic active sites of crystalline cobalt oxyhydroxides for oxygen evolution reaction, *Nat. Commun.*, 2022, **13**, 6650.